

Characterization and potential toxicity of asbestiform erionite from Gawler Downs, New Zealand

JANKI PRAKASH PATEL^{1,*†‡}, MARTIN BROOK¹, MELANIE KAH¹, AYRTON HAMILTON¹,
MARIA CRISTINA GAMBERINI², CARLOTTA ZOBOLI², ENRICO MUGNAIOLI³, DANIELE MALFERRARI⁴,
RICCARDO FANTINI⁴, ROSSELLA ARLETTI⁴, AND ALESSANDRO F. GUALTIERI⁴

¹School of Environment, University of Auckland, Private Bag 92019, Auckland 1010, New Zealand

²Department of Life Sciences, University of Modena and Reggio Emilia, Via G. Campi 103, 41125 Modena, Italy

³Department of Earth Sciences, University of Pisa, Via S. Maria 53, 56126 Pisa, Italy

⁴Department of Chemical and Geological Sciences, University of Modena and Reggio Emilia, Via G. Campi 103, 41125 Modena, Italy

ABSTRACT

Erionite is the name for a zeolite mineral series originating from diagenesis or hydrothermal alteration of volcanic rocks. The particular erionite “species” is based on the dominant extra-framework cation, erionite-Ca, erionite-K, or erionite Na. Irrespective of the species, erionite can display a fibrous/asbestiform morphology and has been linked with cases of malignant mesothelioma, a disease typically associated with asbestos exposure. Characterization of new discoveries of erionite is therefore important to assess any potential exposure hazards. This study describes a new asbestiform erionite from vesicles within the Upper Cretaceous Mt. Somers Volcanics Group (MSVG), Canterbury, New Zealand. The erionite is within the Hinds River Dacite, the youngest unit within the MSVG at Gawler Downs, ~100 km west of Christchurch, in the foothills of the Southern Alps. A multi-analytical approach was taken to analyze the sample which included micro-Raman spectroscopy, thermogravimetric analysis, electron microscopy, electron microprobe analysis, and X-ray powder diffraction with the Rietveld method. Results confirmed the mineral as fibrous erionite-K. The chemical composition of the mineral is unique due to the presence of higher levels of Mg. While Fe was also identified, this was due to smectite flakes occurring on the surface of the erionite fibers. According to the World Health Organization (WHO) respirable mineral fiber definition, where length $\geq 5 \mu\text{m}$, width $\leq 3 \mu\text{m}$, and aspect ratio (L/w) $\geq 3:1$, the Gawler Downs erionite fibers are respirable, while the fibers themselves exceed respirable thickness. In addition to morphology, a value for the potential toxicity model was computed to be 2.28 for the Gawler Downs erionite. This is similar to those of other carcinogenic erionites from Karain, Turkey (2.33), and Nevada, U.S.A. (2.28). Taken together, results indicate Gawler Downs erionite represents an environmental hazard. Nevertheless, further investigation is required to determine potential environmental exposure pathways by which erionite may become airborne and assess the actual environmental risk in the Gawler Downs area.

Keywords: Erionite, asbestos, crystal structure, toxicity, carcinogenicity; Microporous Materials: Crystal-chemistry, Properties, and Utilizations

INTRODUCTION

Erionite is a widespread natural zeolite (framework type ERI) with the ideal chemical formula $\text{K}_2(\text{Ca}_{0.5}\text{Na})_7[\text{Al}_9\text{Si}_{27}\text{O}_{72}] \cdot 28\text{H}_2\text{O}$ (Passaglia and Sheppard 2001). The name erionite comes from the Greek $\epsilon\rho\iota\omega\upsilon$ = wool because this fibrous zeolite sometimes presents a woolly appearance (Gottardi and Galli 1985). Erionite is included in the ABC-6 family (Gottardi and Galli 1985) and displays a periodic building unit (PerBU) consisting of a hexagonal array of planar 6-membered rings of (Si,Al)O₄ tetrahedra (T6-rings) related by pure translations along the *a*- and *b*-axes (Gualtieri et al. 1998; Baerlocher et al. 2007). Its symmetry is hexagonal with space group *P6₃/mmc* and unit-cell parameters

a ~ 13.15 Å, *c* ~ 15.05 Å. In the stacking sequence of erionite, neighboring T6-rings are connected through tilted 4-rings along [001] following the AABAAC... sequence. The framework is characterized by three types of cavities: the cancrinite cage ([4⁶5] polyhedra), double 6-ring (D6R) cages (hexagonal prism, [4⁶2] polyhedron, formed by two “A” 6-rings), and columns of erionite cavities ([4¹²6⁵8⁶] polyhedral) between the “B” or “C” 6-rings (Staples and Gard 1959; Gottardi and Galli 1985; Armbruster and Gunter 2001; McCusker et al. 2001). Erionite has a large chemical variability with the three most abundant species: erionite-Na, erionite-K, and erionite-Ca (Gualtieri et al. 1998; Passaglia et al. 1998). K⁺ cations are located at the center of the cancrinite cages, while Na⁺, Ca²⁺, Mg²⁺, and water molecules occupy the erionite cavities and are distributed on sites located on the symmetry axis (Gualtieri et al. 1998). Alberti et al. (1997) found that in the erionite cavities, there are three partially occupied positions Ca1, Ca2, Ca3, and each is coordinated with water molecules. One additional cation site was observed at a special position (½, 0, 0)

* Corresponding author E-mail: janki.patel@auckland.ac.nz. Orcid <https://orcid.org/0000-0002-3118-4282>

† Special collection papers can be found online at our website in the Special Collection section.

‡ Open access: Article available to all readers online. This article is CC-BY-NC-ND.

by Ballirano et al. (2009) and Giacobbe et al. (2023) in erionite-K and labeled as K2. This site corresponds to the K site found by Schlenker et al. (1977) in dehydrated erionite-Ca and to the Ca4 site found by Gualtieri et al. (1998) in some natural erionite-Ca samples (Ballirano and Cametti 2012; Ballirano et al. 2017).

In nature, erionite occurs in two genetic environments: (1) diagenetic as alteration of vitroclastic rocks (with mean $R = [\text{Si}+\text{Al}]/\text{Si} = 0.78$). In tuffaceous rhyolites and altered tuffs, both hydrologically closed or open systems/autoclave genesis are observed (Gottardi and Galli 1985). For this environment, formations in lacustrine beds and burial diagenesis are also possible genetic mechanisms; (2) hydrothermal (with mean $R = 0.75$) in the vugs of altered volcanic rocks such as basalts, andesites, limburgites, and many more (Passaglia et al. 1998; Passaglia and Sheppard 2001).

The crystal habitus of erionite observed in both diagenetic and hydrothermal environments are manifold, as evidenced by the countless number of terms used in literature to describe erionite associations, including prismatic, acicular, needles, rods, fibrous, fibers, hair-like, woolly, bundles, radiating clusters (Dogan et al. 2008; Giordani et al. 2017). A simplified classification of the erionite crystal habit is: (1) stocky hexagonal prisms usually terminated with basal pinacoids like the diagenetic erionite crystals from Durkee, Oregon, U.S.A. (Gottardi and Galli 1985); (2) acicular hexagonal prisms with regular or irregular basal terminations. A nice example of hydrothermal acicular erionite can be found at the Niigata Prefecture, Japan (Harada et al. 1967); (3) fibrous hexagonal prisms or fiber bundles with regular or irregular basal terminations like the erionite crystals from Oregon, U.S.A. (Gottardi and Galli 1985), and most of the Turkish (Cappadocia) and American diagenetic erionite samples (Van Gosen et al. 2013); (4) aggregates of stocky/fibrous hexagonal prisms (amygdaloid) like the diagenetic erionite samples from Bowie, Arizona, U.S.A. (Gottardi and Galli 1985); (5) woolly asbestiform fiber bundles like the flexible hair-like fibers having a width of about $0.1 \mu\text{m}$, extremely variable lengths and sometimes curious “brush-like” terminations observed in the erionite samples from Lessini Mounts in Italy (Giordani et al. 2016). It should be noted that erionite intergrowth with offretite (framework type OFF) is very common because of the close similarity of the crystal-structure and crystal-chemical assemblages of these two zeolites. In fact, offretite has an ideal chemical formula of $\text{K}_2(\text{Ca}_{0.5}, \text{Na})_4\text{Mg}_2[\text{Al}_{10}\text{Si}_{26}\text{O}_{72}] \cdot 32\text{H}_2\text{O}$ (Passaglia and Sheppard 2001) and hexagonal symmetry with space group $P\bar{6}m2$ and unit-cell parameters $a \sim 13.30 \text{ \AA}$, $c \sim 7.60 \text{ \AA}$. Passaglia et al. (1998) reported that the two zeolites have well-defined compositional fields, and the crystal chemistry of the Mg cation is a major factor in controlling their crystallization.

Erionite can have a fibrous or asbestiform morphology, and its exposure has been linked to cases of malignant mesothelioma, a fatal and aggressive cancer (Bariş et al. 1996). Importantly, fibrous/asbestiform erionite appears to be even more carcinogenic than the six regulated asbestos minerals (Wylie 2017). The first health issues regarding erionite exposure and mesothelioma were noted in Cappadocia (Turkey), and more recently, occupational exposure issues have emerged in the U.S.A. (Van Gosen et al. 2013). The International Agency for Research on Cancer (IARC) has classified erionite as a Group 1 carcinogen (IARC

1997). Nevertheless, when erionite fibers remain undisturbed in rock and/or soil, they are assumed not to pose a risk to human health. Airborne fibers, however, may be considered hazardous if they satisfy the following size requirements set out by the World Health Organization to be considered respirable: length $\geq 5 \mu\text{m}$, width $\leq 3 \mu\text{m}$, and aspect ratio (L/w) $\geq 3:1$ (WHO 1986, 1997).

In New Zealand, erionite has been found in surface rock exposures at numerous locations throughout both the North and South Islands, including (from north to south) Kaipara, Auckland, Taupo Volcanic Zone, Banks Peninsula, and the Moeraki coast (Patel et al. 2022). New Zealand is one of several high-income countries with an elevated incidence of malignant mesothelioma cases (2.6 per 100 000), thought to result from occupational exposure to airborne asbestos fibers. Thus, understanding the distribution and character of erionite in New Zealand and assessing the potential exposure risk for the population is crucial, as residential land development is occurring in some areas where erionite is known to be present (Brook et al. 2020). To this aim, a systematic long-term study of the mapping and crystal chemical characterization of erionite in New Zealand started in 2020 (Brook et al. 2020; Patel and Brook 2021; Patel et al. 2022).

In this scenario, our work describes for the first time the crystal chemistry and morphology of an outstanding asbestiform erionite from Gawler Downs, New Zealand, to assess if this fiber can represent an environmental hazard. The work takes advantage of a suite of complimentary experimental techniques to comprehensively characterize the sample and predict its potential toxicity and carcinogenicity.

SOURCE OF THE SAMPLE AND GEOLOGICAL OVERVIEW

The sample site (GD4a) lies within the Gawler Downs, which are foothills of the Southern Alps, 35 km northwest of Ashburton on New Zealand’s South Island (Fig. 1). This is a landscape of downlands, comprising subdued landscapes of undulating smooth hills or broad ridges dissected by steep gullies draining to broad floodplains. Gawler Downs is composed of the erosional and block-faulted remnants of a suite of Late Cretaceous calc-alkaline volcanic rocks, the Mount Somers Volcanics Group (MSVG; Oliver and Keene 1989). These volcanic flows and domes are preserved discontinuously in the eastern foothills of the Southern Alps, northeastwards from the Rangitata River gorge to the Malvern Hills (Fig. 1). This $\sim 18\,000 \text{ km}^2$ volcanic center represents the youngest (ca. 99–96 Ma; van der Meer et al. 2017) known calc-alkaline volcanism in Zealandia during its Paleozoic-Mesozoic Gondwana active margin setting (Oliver and Keene 1989; Tappenden 2003; van der Meer et al. 2017). Erupted magma volumes are thought to have been similar to the present-day Taupo Volcanic Zone (Tappenden 2003), and MSVG units intruded and overly Torlesse meta-sediments of the Permian to Late Triassic Rakaia Terrane (Smith and Cole 1996). Paleogene to Holocene cover strata are interpreted to overlay most of the MSVG deposits, which also continue under the Canterbury Plains and offshore (Field and Browne 1989).

The MSVG can be divided into intermediate/basic (basaltic andesite to dacite) and rhyolitic/ignimbrite rocks, although Oliver and Keene (1989) and Smith and Cole (1996) report much more detailed and contrasting stratigraphic nomenclatures. Nevertheless, at the main MSVG occurrence in the Mt. Somers

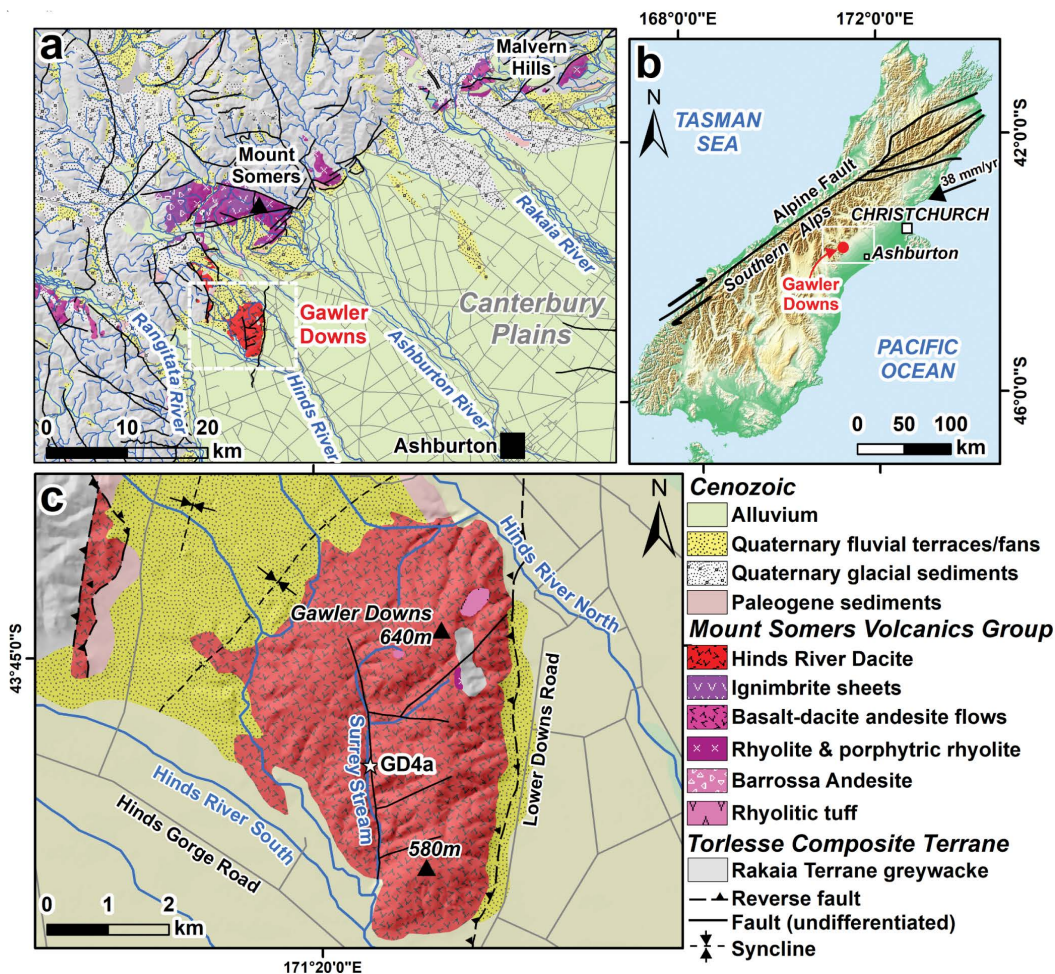


FIGURE 1. (a) Geological Map of the Mount Somers Area. (b) Map of the South Island of New Zealand, indicating the Gawler Downs study area. (c) Geological Map of Gawler Downs, with sampling point.

area to the north of Gawler Downs (Fig. 1a), the oldest units consist of both massive and bedded rhyolitic tuff, recording the first explosive silicic volcanism at Mt. Somers. Barrossa Andesite crops out over ~2 km² to the north and northwest of Mt. Somers, overlying Surrey Hills Tuff, and in some places directly overlying Torlesse Greywacke (Smith and Cole 1996). Barrossa Andesite forms lava flows up to 80 m thick and is overlain by younger ignimbrite, rhyolite, and tuffs. Where fresh, the ignimbrite units are a moderately indurated, black, glassy, porphyritic vitrophyre that contains up to 15% lithic fragments. It weathers to a friable, green-gray glassy sand and, in extreme situations, to a green bentonite (Smith and Cole 1996). Silica contents decrease stratigraphically upwards toward dacites and andesites, the Hinds River Dacite being the youngest MSVG unit (Oliver and Keene 1989; Smith and Cole 1996).

At Gawler Downs, the Hinds River Dacite covers most of the area, although the outcrop is sparse (Figs. 1b and 1c), aside from valley floors where the GD4a sample was extracted from, close to Surrey Stream (Fig. 1c). The Hinds River Dacite includes glassy and porphyritic dacite flows and dikes. The dacites are dominated by heavily weathered, often rubbly and amygdaloidal

flows (Tappenden 2003), and the basal beds of the dacite show considerable hydrothermal alteration as a result of the hot dacite lava having flowed over the wet, bedded tuff. The tuff present at Gawler Downs underlies the Hinds River Dacite and outcrops to the east of the Gawler Downs trig point as pale green and pink laminated fine siltstone. The mineral assemblage consists of plagioclase, sanidine, quartz, biotite, garnet, and opaque minerals (ilmenite), which indicates a relationship between the tuff and the overlying volcanic units (Tappenden 2003). A small outcrop of tuff underlying the Hinds River Dacite also occurs near the headwaters of Surrey Stream, southwest of the Gawler Downs trig station (Oliver 1977; Fig. 1c).

The site of GD4a occurrence consisted of a road cutting up to 2 m in height and 100 m across (Fig. 2a). The dacite flows and tuff layers within the outcrop had been hydrothermally altered and infilled with silica (agate, chalcedony, opal, and quartz), clays and zeolites, as well as silicification and veining (Field and Browne 1989; Oliver and Keene 1989). The rock sampled had a phaneritic texture and was a moderately weathered ash deposit that had a vesicle ~3 cm present, infilled with the fibrous erionite (Fig. 2b). Smaller vesicles up to 5 mm wide were not infilled.

SAMPLING PROCEDURE

The sampling method engaged for collecting the erionite samples involved surveying the volcanic rock for vesicles in-filled with a fibrous material. Using a geological hammer, the vesicles found were dislodged from the host rock and placed in a plastic bag; approximately ~400 g of the host rock was also taken. Samples were stored in separate plastic bags to prevent cross contamination and reduce any adverse health effects from fibers becoming airborne and inhaled during transportation to the labs. For analysis, samples of the fibers were prepared by drying and cryo-milling to crush the powder finely. Fibrous bunches were also used for scanning electron microscopy (SEM) as well as homogenized while mixed with acetone to disperse the fibers on carbon tape.

METHODS

Raman analyses were conducted with a confocal micro-Raman LabRAM HR evolution (Horiba Jobin Yvon, Edison, U.S.A.), equipped with a red He-Ne laser at 532 nm (1 μm size spot), notch filters to eliminate the exciter, detector CCD front illuminated open electrode multi-pin phased, with $1024 \times 256 \times 16$ pixels, cooled by a Peltier system. Spectra were recorded in backscattering after focalization in several positions within a small area of the sample (ca. $100 \times 100 \mu\text{m}$). The maximum laser power employed was 20 mW, and the recording time for a good signal-to-noise ratio was 10 s for 50 accumulations. Furthermore, LabSpec6 was used for the spectra elaboration.

Thermogravimetric (TGA) measurements were carried out with a Seiko SSC 5200 thermal analyzer coupled with a quadrupole mass spectrometer (ESS, GeneSys Quadstar 422) to detect the volatiles evolved during thermal reactions (MSEGA). Experimental conditions were: heating rate: 20 $^{\circ}\text{C}/\text{min}$; thermal range: 25–850 $^{\circ}\text{C}$; purging gas: ultrapure helium, flow rate: 100 $\mu\text{L}/\text{min}$. Mass analyses were carried out to detect the possible emission of H_2O , CO_2 , and SO_2 as the most likely gaseous compounds resulting from dehydration and/or thermal decomposition of impurities; for this purpose, intensity as a function of temperature was measured for the m/z signals 18, 44, and 64 for H_2O , CO_2 , and SO_2 , respectively, where m/z is the dimensionless ratio between the mass number and charge of an ion.



FIGURE 2. (a) Overview of the road cutting where sampling took place. (b) Image of the GD4a vesicle filled with fibrous erionite.

The morphological observation of the samples was carried out by a Scanning Electron Microscope (SEM) using JSM-6020PLUS/LA (JEOL, Hillsboro, U.S.A.) equipped with an energy-dispersive X-ray (EDX) spectrometer (Oxford INCA-350) and Field Emission Gun Scanning Electron Microscope (FEG-SEM) FEI Nova NanoSEM 450 FEG-SEM. An aliquot of raw sample was fixed on an aluminum stub with double-stick carbon tape and coated with a thin film of carbon (10 nm of thickness) using a Carbon Coater-Balzers CED-010. A series of representative SEM images were obtained by secondary electron (SE) signal and analyzed using ImageJ software.

For the electron microprobe analysis (EMPA), quantitative wavelength-dispersive spectrometry (WDS) microanalyses were performed on a few sample aggregates embedded in resin disks of 1 inch and polished at 1 μm . The employed instrument was a JEOL 8200 Super Probe with W hairpin type filament, equipped with five wavelength-dispersive spectrometers. Analyses were performed with atomic number resolution on BSE (Z): less/equal than 0.1 (CuZ), accelerating voltage of 15 kV, detectable wavelength of 0.087 to 9.3 nm, specimen current of 5 nA, peak-count time of 30 s, and background-count time of 10 s. The instrument is also equipped with EDX system characterized by a detectable element range: Na to U, energy resolution: 144 eV, and lithium (Li)-doped silicon single-crystal semiconductor detector. Several spot analyses (31) were collected to gain good analytical statistics because fibrous erionite bundles could be contaminated by other mineral phases, and the chemical formula could be biased. Online Materials¹ Figure S1 reports the points of the fiber bundles where the selected points were taken. Spot analyses were also conducted along the elongated fibers to verify chemical homogeneity. Out of the 31 collected points, 11 were selected for the calculation of the chemical formula. The statistics of these points are reported in Online Materials¹ Table S1.

High-resolution transmission electron microscopy (HRTEM) imaging and three-dimensional electron diffraction (3DED) were performed with a JEOL JEM-F200 Multipurpose, working at 200 kV and equipped with a Schottky field emission gun (FEG) and a silicon drift detector (SDD) for EDX. HRTEM data were acquired by a Gatan RIO-16 CMOS camera ($4k \times 4k$ pixel) and analyzed by Gatan Digital Micrograph software. EDX data were collected and quantified by JEOL software. Electron diffraction data were recorded by an ASI Cheetah hybrid-pixel detector working in sequential mode at 24 bit. 3DED data were collected in steps of 1° , with a nanobeam of about 30 nm obtained by inserting a 10 μm condenser aperture (Gemmi et al. 2019). Crystal tracking was performed in STEM mode. The beam was processed by a NanoMEGAS Topspin device with a precession semi-angle of 1° (Mugnaioli et al. 2009). Exposure time for each diffraction pattern was 1 s. Camera length was 250 mm, equivalent in the direct space to a maximum resolution of about 0.7 \AA . 3DED data were analyzed by the software PETS2 (Palatinus et al. 2019).

The specific surface area (SSA) of the sample was determined by N_2 adsorption/desorption isotherms using the ChemiSorb 2750–Micromeritics instrument. Adsorption data were processed at the liquid nitrogen temperature (about -196°C) following the standard Brunauer, Emmet and Teller (BET) method (Naderi 2015), and surface area was calculated as the average of three independent measurements on three different portions (~500 mg) of the sample. Before each measurement, the sample was conditioned at 50 $^{\circ}\text{C}$ under N_2 flow for about 30 min.

The ζ potential was determined both in distilled water and in organic Gamble's modified solution (Gulberg et al. 1998), the latter reproducing the intracellular alveolar lung fluid of the macrophage phago-lysosome environment. The measurements were conducted at pH = 4.5 and 7.4 at 37 $^{\circ}\text{C}$ (the temperature of the body), using a ZetasizerNano Series instrument (Malvern). The pH of the suspensions was monitored using a Crison Series 2000 instrument.

For the structure refinement, X-ray powder diffraction (XRPD) data collected with a lab source and synchrotron radiation were merged. The same powder sample used for the two experiments was obtained by cryogenic milling using a Retsch mixer mill MM 400 (Düsseldorf, Germany) equipped with two milling jars (35 mL) made of steel accompanied with a steel milling ball. The lining of the jar and balls is made of polytetrafluoroethylene (PTFE), which serves to prevent contamination of the sample with metals from the jar and balls during milling. Following the procedure described in Di Giuseppe et al. (2021a), the jars are filled with the sample in liquid nitrogen. When cooled, the jars are mounted in the mixer mill. During operation, jars oscillate from side to side with a pre-set frequency. For the experiment, the jars were loaded with 1 g of raw material, and an oscillation frequency of 30 Hz was applied for 5 min. The lab experiment was conducted using a Bragg-Brentano PANalytical X'Pert Pro diffractometer, with a vertical circle Θ - Θ goniometer (240 mm radius), $\text{CuK}\alpha$ radiation, 40 kV and 40 mA, and a Real Time Multiple Strip detector. Data were collected in reflection geometry with $1/2^{\circ}$ fixed divergence and anti-scatter slits and 0.02 rad soller slits. An integrated step

scan of the detector of $0.013^\circ 2\theta$ was used with counting statistics of 180 s/step from 5 to $120^\circ 2\theta$. Synchrotron X-ray powder diffraction (XRPD) pattern for the structure refinement of the sample was collected at the Material Characterization by X-ray Diffraction Beamline (MCX), the synchrotron facility of ELETTRA (Trieste, Italy). The employed detector was a 4-circle Huber goniometer with a crystal analyzer/scintillation detector system, preceded by two slits with 200 and 300 μm vertical apertures. Measurements were performed at room temperature in transmission geometry using a borosilicate capillary ($\varnothing = 0.8 \text{ mm}$) and a fixed wavelength of 0.8263 \AA (i.e., 15 keV), in the $2\text{--}65^\circ 2\theta$ range, with data step of $0.008^\circ 2\theta$ and counting rate of 2.5 s per step. The Rietveld (Rietveld 1969) structure refinement using the two data sets was accomplished with the GSAS package (Larson and Von Dreele 2004) and its graphical interface EXPGUI (Toby 2001). The starting structural model of erionite-K of Ballirano et al. (2009) was used and substantially modified during the refinement process. The background was modeled with a 12-term Chebyshev function. The diffraction peak profiles were modeled using a pseudo-Voigt function with one Gaussian and two Lorentzian coefficients. The refinement included the unit-cell parameters, the phase fraction, the atomic coordinates, and the atomic site occupancies for extra-framework positions kept fixed to the value of atoms per formula unit determined by the EPMA data. Isotropic atomic displacement parameters were also refined in the later stages of the procedure. Soft constraints on tetrahedral bond lengths were imposed and used as additional observations, with their weight progressively reduced to five in the later stages of the procedure. Difference Fourier maps were repeatedly calculated from the refined model and were useful for the location of residual electron density corresponding to extra-framework cations or H_2O molecules.

DETERMINATION OF THE TOXICITY/CARCINOGENICITY POTENTIAL OF THE SAMPLE USING THE FPTI MODEL

The Fiber Potential Toxicity Index (FPTI) model (Gualtieri 2018, 2021) was used to calculate the toxicity/carcinogenicity potential of the sample GD4a. The following parameters of the model are considered: morphometric parameters (mean fiber length and diameter, crystal habit and curvature, density, hydrophobic character, specific surface area), chemical parameters (iron content, content of ferrous iron, surface iron and its nuclearity, content of metals other than iron), biodurability related parameters (dissolution rate, rate of iron dissolution/release, rate of silica dissolution/release, rate of release of metals from the fiber), surface reactivity (ξ potential, aggregation state of the fibers in suspension, cation exchange capacity for fibrous zeolite species). For each parameter, a score is assigned depending on its measured value, susceptibility in inducing adverse effects, and weight (Gualtieri 2018). The FPTI_i is calculated according to the equation (Gualtieri 2018):

$$\text{FPTI}_i = \sum_{i=1}^n w_1 w_2 T_i$$

with $w_1 = 1/H$ weight of the parameter according to its hierarchy H ; $w_2 = 1/U$ weight of the parameter according to the uncertainty U of its determination; $T_i =$ class value of the parameter i of the model. All the details of the model are explained in Gualtieri et al. (2021) and the WebFPTI manual available at <http://fibers-fpti.unimore.it/FPTI/> that includes the calculation of the errors associated with each parameter.

RESULTS AND DISCUSSION

Chemical and morphological characterization

The TGA curve and its first derivative (DTG) show two distinct reactions (Fig. 3a), each of which occurs in two steps. The first reaction takes place between 25 and 350 $^\circ\text{C}$ with maximum reaction rates at 68 $^\circ\text{C}$ (step I, maximum on the DTG curve) and at about 165 $^\circ\text{C}$ (step II, shoulder on the DTG curve), with an

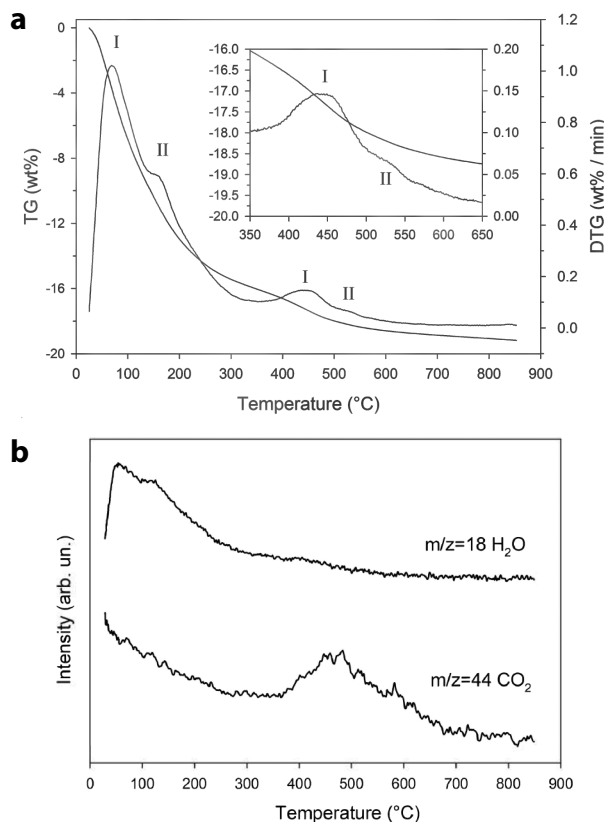


FIGURE 3. Results of the thermal analysis of sample GD4a up to 900 $^\circ\text{C}$. (a) Thermogravimetric analysis (TGA) and its first derivative (DTG); (b) analysis of the gases evolved during thermal reactions (MSEGA) measured using a quadrupole mass spectrometer.

overall mass change of 16.04 wt%. The second reaction, which is much less pronounced, is observed between 350 and 650 $^\circ\text{C}$; the DTG curve shows a maximum (step I) at 435 $^\circ\text{C}$ and a shoulder (step II) at about 525 $^\circ\text{C}$, with a total mass change of 2.71 wt%. No further changes are observed thereafter, and the overall mass changes at 800 $^\circ\text{C}$ is 19.06 wt%. The MSEGAs curves show the release of H_2O ($m/z = 18$) in the first reaction and H_2O and CO_2 ($m/z = 44$) in the second reaction (Fig. 3b). The water released in both reactions is attributable to the removal of water molecules within the zeolitic channel (Gottardi and Galli 1985; Ballirano et al. 2009; Ballirano and Cametti 2012; Bloise et al. 2016, 2017). This reaction develops over a wide thermal range (up to 450 $^\circ\text{C}$: Ballirano et al. 2009), and the pattern of development, as well as the amount of total water released, depends essentially on the type and number of cations present in the zeolitic channels. The release of CO_2 is probably related to the presence of carbonaceous impurities, as suggested by the higher temperature at which the reaction begins, as better shown by the MSEGAs curve (Fig. 3b). Because of the partial overlap of the water and carbon dioxide release, it is not possible to measure exactly the amount of zeolitic water released in this second reaction; however, considering the temperature of the start and end of gas release evidenced by the MSEGAs curve, we can estimate a value of about 1.6 wt% of water. Consequently, the total amount of zeolitic water for sample GD4a can be estimated to be about 17.7 wt%, a value in

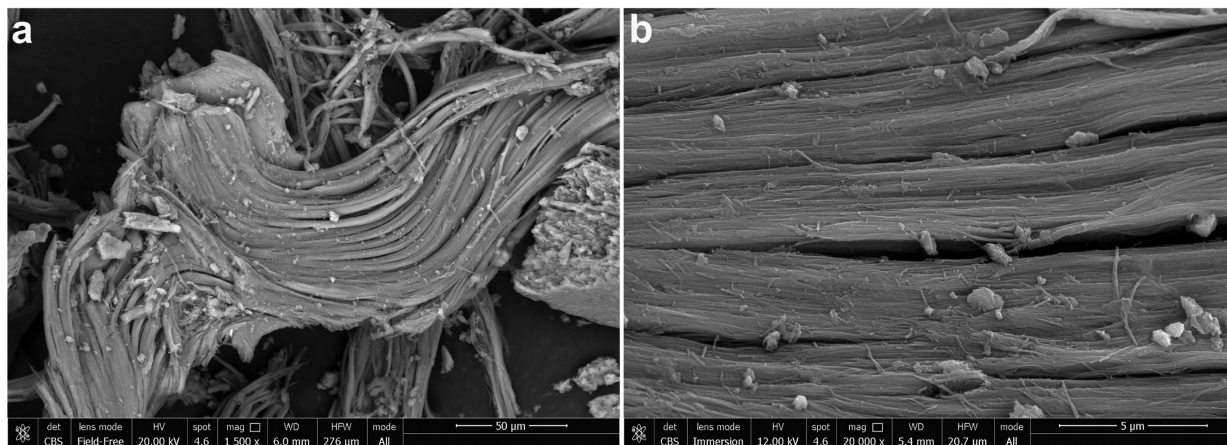
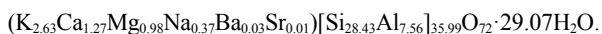


FIGURE 4. FEG-SEM images of the GD4a erionite sample showing the asbestiform crystal habit. (a) Low-magnification picture; (b) high-magnification image of the previous fiber bundle.

good agreement with that determined in the above-mentioned studies (Gottardi and Galli 1985; Ballirano et al. 2009; Ballirano and Cametti 2012; Bloise et al. 2016, 2017)

The chemical formula calculated for sample GD4a using EMPA is:



Iron has been detected and measured with variable concentration but was intentionally excluded from both the framework and extraframework contents because it is assumed not to belong to the erionite structure, as explained in Gualtieri et al. (2016) and discussed below.

The measured external surface area is 20.6(0.4) m²/g. This value is higher than others documented in the literature data [8.14 m²/g (Giordani et al. 2022); 10.1 m²/g (Pacella et al. 2021)], likely because the fibers of the GD4A sample are smaller and the

TABLE 1. SEM morphometric analysis of GD4a fibers

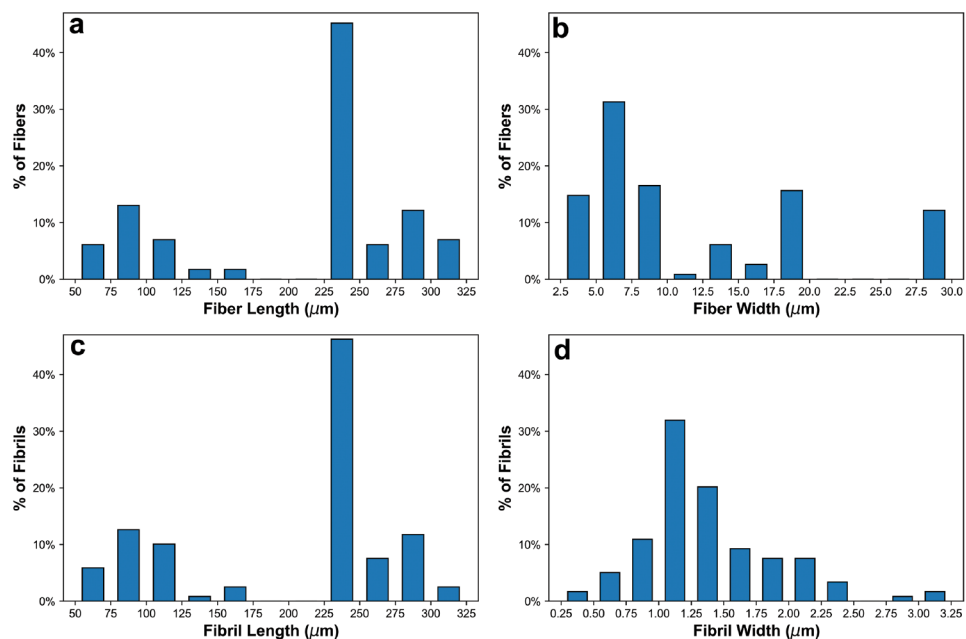
	Min	Max	Mean	25th percentile	75th percentile
L_f (µm)	50.71	307.96	210.47	111.25	248.33
W_f (µm)	2.70	29.93	12.07	6.02	18.10
L_f/W_f	3.95	99.34	25.40	9.89	33.31
L_f (µm)	50.71	307.96	206.82	111.25	243.93
W_f (µm)	0.34	3.15	1.36	1.03	1.61
$W_{f,TEM}$ (µm)	0.12	1.50	0.39		
$L_f/W_{f,TEM}$	25.10	717.44	171.05	99.33	212.25

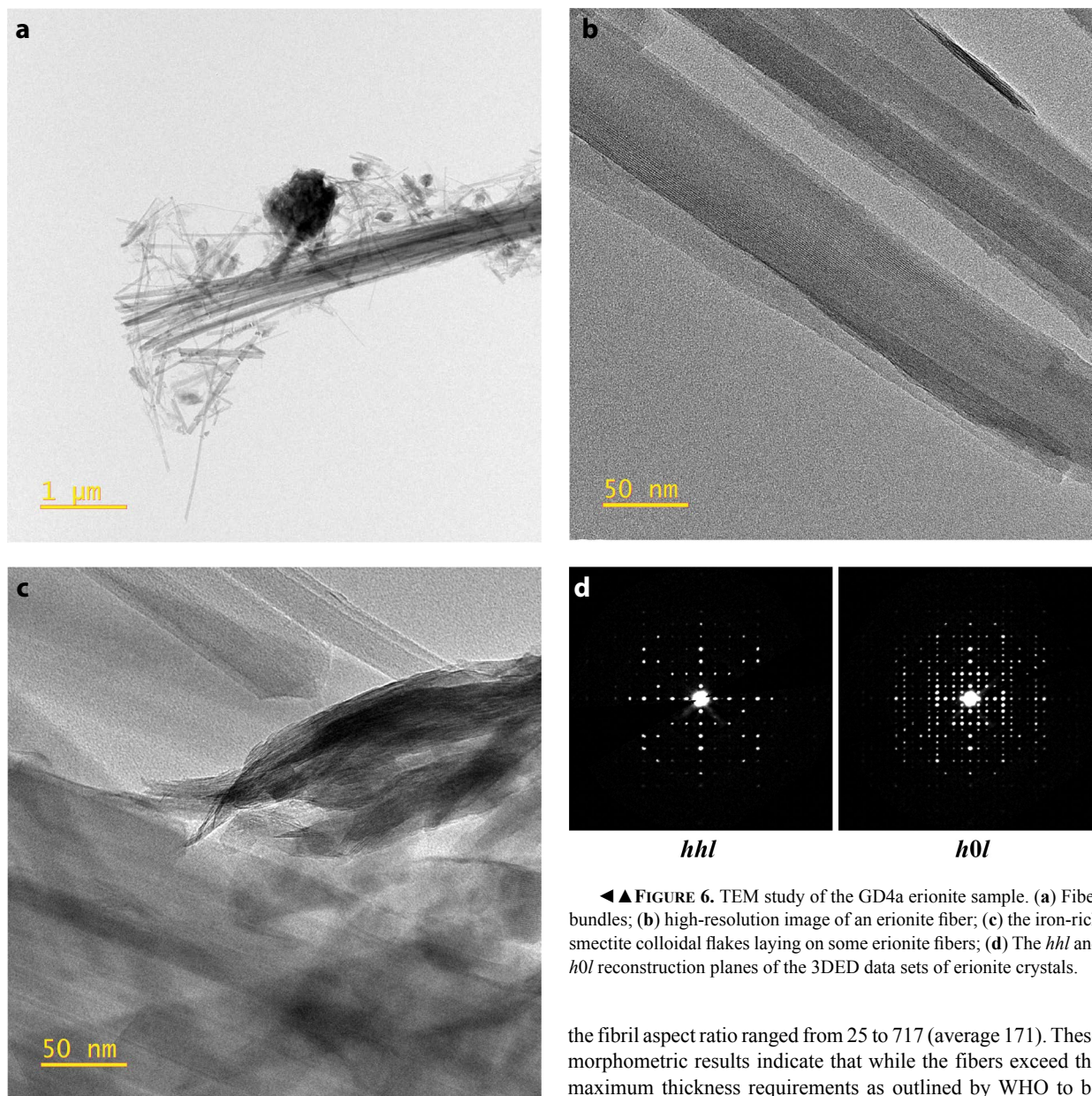
Notes: L_f (fiber length); W_f (fiber width); L_f (fibril length); W_f (fibril width); $W_{f,TEM}$ (fibril width as determined from high-resolution TEM data); L_f/W_f (aspect ratio for fiber); $L_f/W_{f,TEM}$ (aspect ratio for fibril).

specific surface is higher than that of the other erionite samples.

The morphology of sample GD4a was observed using SEM and TEM and consists of an asbestiform crystal habit made up of long curly bundles (Fig. 4a) of nanometric erionite fibrils (Fig. 4b). A morphometric analysis was conducted using ~100 measurements taken from SEM and TEM images and is

FIGURE 5. Histograms of the measured fiber sizes for GD4a. (a) Fiber length (L_f); (b) fiber width (W_f); (c) fibril length (L_f); (d) fibril width (W_f).





◀▲ **FIGURE 6.** TEM study of the GD4a erionite sample. (a) Fiber bundles; (b) high-resolution image of an erionite fiber; (c) the iron-rich smectite colloidal flakes laying on some erionite fibers; (d) The *hhl* and *h0l* reconstruction planes of the 3DED data sets of erionite crystals.

displayed in Table 1 and summarized in a series of histograms as shown on Figure 5.

The fibers had a woolly appearance, with the length varying between 50 to 308 μm (average 210 μm). The results were similar for both fiber and fibril length. The width ranged between 2.7 to 30 μm (average 12 μm) for the bundles of fibers, however, over 30% of the width fell between 5–7.5 μm. The fibrils typically had a much smaller width, ranging between 0.34 to 3 μm (average 1.36 μm). The mean size of the fibrils measured from the TEM data is even smaller (0.39 μm) because what appears as a single fiber at SEM resolution often results as a bundle of smaller fibers. As opposed to the morphometric data for the lengths and fiber width, the distribution for fibril width was unimodal, with ~50% of the fibrils between 1 to 1.5 μm. The aspect ratio for fibers ranged between 4 to 99 (average 25), and

the fibril aspect ratio ranged from 25 to 717 (average 171). These morphometric results indicate that while the fibers exceed the maximum thickness requirements as outlined by WHO to be respirable, the fibrils are thin and have the 3:1 aspect ratio to be considered a potential hazard (WHO 1986, 1997).

TEM morphometric measurements are in agreement with SEM data and show that the sample is mostly composed of elongated fibers and bundles, generally shorter than 50 nm in thickness and with lengths of several micrometers. The fibers are generally bent and tend to form bundles (Fig. 6a). Fibers may undergo beam damage and can stand moderate HRTEM conditions only for a few seconds. They become immediately amorphous when magnification gets above 150–200×. However, HRTEM images clearly show that fibers are crystalline (Fig. 6b). Some of them are single crystals, with a certain bending through the fiber length. When a single crystal, the most recurrently visible interplanar distance is 11.0–11.6 Å, it is always parallel with the long side of the fiber. Sometimes it is possible to see a second interplanar distance perpendicular to the previous one, with

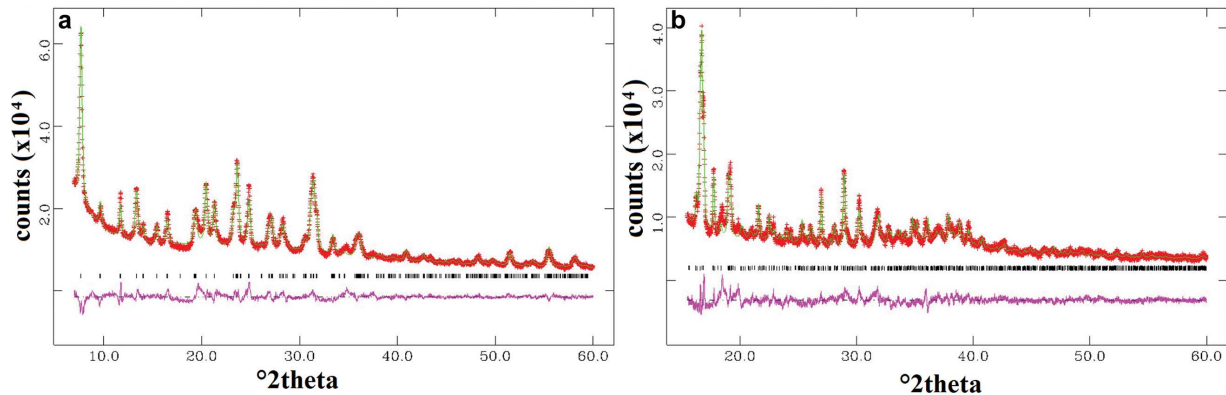


FIGURE 7. Selected regions of the patterns with the observed data points (red), calculated points (green), markers of the erionite reflections, and difference curve (magenta). (a) Lab source; (b) synchrotron source.

value 15.0–15.3 Å, always parallel to the short fiber side. These distances correspond to the cell of erionite, with $d_{100} = 11.2$ Å and $d_{001} = 15.1$ Å. The main direction of fiber growth is then c^* , while it is reasonable to assume hexagonal cross section of the fiber coherent with the $hk0$ plane. Rarely, some fibers show a periodicity of 7.5–7.6 Å. This may be coherent with the offretite cell. However, this cell parameter always appears when the fiber has only 1D resolution, i.e., only the 00 l line is visible in diffraction. In this condition, also erionite would show a periodicity of 7.5 Å, coherently with the presence of the 6_3 screw axis. It is, therefore, the opinion of the authors that all HRTEM images can be explained with an erionite cell. Some fibers show disorder, with more domains growing one next to the other along the fiber length. Sometimes, the occurrence of more domains results in fringed fiber terminations. It is worth noting that this disorder appears not immediately associable with supposed erionite/offretite alternation (as found for other samples in the literature: Gualtieri et al. 1998), which would be better imagined as an order-disorder sequence along c^* , i.e., along the fiber length. In between the fibers, flake-like or lamellar particles are observed (Fig. 6c). This material is scarcely crystalline, and only rarely is it possible to see some very disordered layer sequences with interspacing of about 10–12 Å.

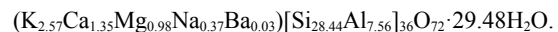
Three 3DED data sets were collected from three different fibers, which appeared well ordered and larger than the average. After the reconstruction, all three data sets resulted in consistency with the erionite cell (Fig. 6d). No significant disorder was observed. The best data set delivered a hexagonal cell with $a = 13.2$ Å and $c = 15.1$ Å. Extinctions are consistent with space group $P6_3/mmc$ and can be recognized in the reconstructed 2D diffraction patterns. The best data set was also used for a tentative ab initio structure determination by direct methods implemented in SIR2014 (Burla et al. 2015). The framework of erionite was immediately detected, together with the clear localization of K and possibly partially occupied Ca/Na ions and water molecules in the cavities.

Energy-dispersive spectroscopy (EDS) spot analyses confirmed that the fibers are mostly made of Si and O. Al is invariably present generally together with K and Ca. Na, Mg, and Cl peaks are also generally detected but are very weak (see Online

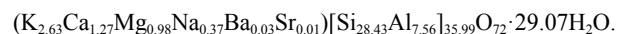
Materials¹ S2). EDS analyses were not performed with an analytical holder, and therefore the peak of Fe is always present, together with Cr and Co. With the present data, we suggest to consider Fe as an artifact when present with <2 wt%. No EDS points from the fibers show an Fe signal higher than 2%. On the other hand, EDS analyses from flake-like material show a considerable increase in Fe, Al, Mg, and sometimes Ca (see Online Materials¹ S2).

To summarize, the TEM study indicates that all inspected fibers are probably erionite, and specifically erionite-K (possibly also erionite-Ca in some cases). They show a high degree of crystallinity and fibrous-asbestiform habit. The source of iron in the sample is not from iron-oxides or hydroxide particles but from flakes of layer silicates, possibly a smectite-rich phase like nontronite, as already observed for other natural asbestiform erionites (Gualtieri et al. 2016).

XRPD data confirmed that the specimen contains about 2 wt% of smectite and illite. Other impurities are below the detection limit of X-ray diffraction. Figure 7 reports the fit obtained by the Rietveld refinement of the GD4a erionite sample, while Online Materials¹ Table S3 reports the refinement statistics, calculated unit cell and structural parameters. Pointing out that the site population of the sites occupied by Mg, Na, Ba, and Al were fixed to the values of the formula calculated from the EPMA data and that Sr was not considered, the chemical composition from the final refinement was



The formula should be compared to that calculated from the EPMA data:



Due to the great disorder of the water molecules, only the oxygen atoms were located, and the hydrogen atoms of the water molecules were not positioned. The relevant bond distances are shown in Table 2. The full set of bond distances and angles are available upon request to the authors.

The two independent tetrahedral sites T1 and T2 are occupied by Si and Al in a disordered way and build the D6R and S6R cages, respectively. The mean bond distances $\langle\text{T1-O}\rangle =$

TABLE 2. Relevant bond distances (Å) calculated from the Rietveld refinement of the GD4a erionite sample

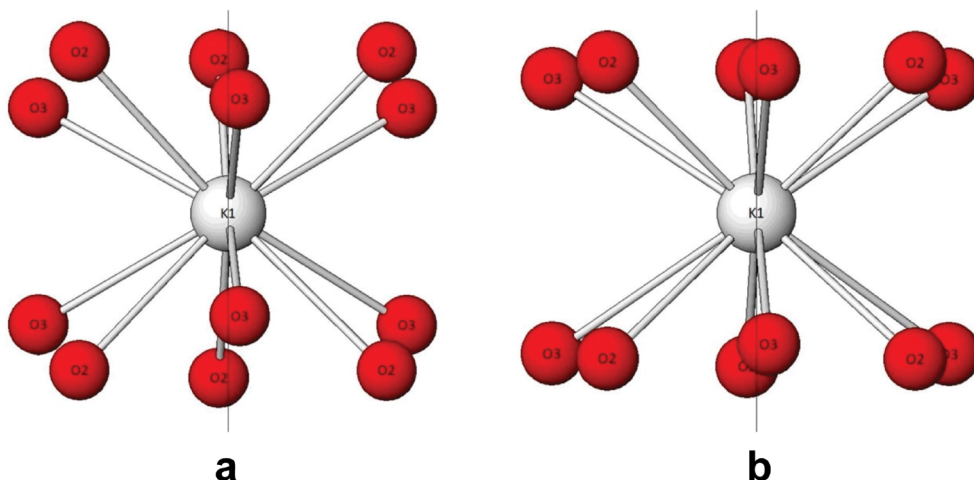
Framework		
T1-O1	1.6290(6)	
T1-O2	1.5990(7)	
T1-O3	1.6941(6)	
T1-O4	1.6283(8)	
Mean	1.6376	
T2-O1 ×2	1.6475(8)	
T2-O5	1.6759(7)	
T2-O6	1.6154(7)	
Mean	1.646575	
Extraframework		
Ca1-OW1 ×2	2.9793(10)	K1-O2 ×6 3.1539(11)
Ca1-OW1	2.9792(10)	K1-O3 ×6 3.1601(11)
Ca1-OW2 ×3	2.4435(9)	
Ca1-OW6 ×2	2.5054(10)	K2-O1 ×4 3.2246(11)
Ca1-OW6	2.5055(10)	K2-O4 ×2 3.1283(11)
		K2-OW1 ×4 3.3840(12)
Na1-OW2 ×3	2.4435(9)	K2-OW3 ×4 3.0109(11)
Na1-OW6 ×2	2.5054(10)	
Na1-OW6	2.5055(10)	K3-O5 ×3 3.1059(13)
		K3-O6 ×3 3.5174(13)
		K3-OW3 ×6 3.1010(13)
Ca2-OW2 ×2	2.4276(9)	
Ca2-OW2	2.4275(11)	
Ca2-OW3 ×6	2.6542(12)	Mg1-OW3 ×6 2.092(1)
Ca2-OW6 ×2	2.6524(10)	Mg1-OW5 ×3 2.423(1)
Ca2-OW6	2.6525(10)	Mg1-OW7 ×3 1.897(1)
Ba2-OW3 ×6	2.6542(12)	
Ba2-OW6	3.0287(10)	
Ba2-OW6 ×2	3.0286(10)	
Ba2-OW6 ×2	2.6524(10)	
Ba2-OW6	2.6525(10)	

1.6376 Å, and $\langle T2-O \rangle = 1.646575$ Å indicate a negligible difference between the mean (T-O) distances of the two tetrahedral sites, with a very small preference of Al for T2 compared with T1 (0.14). Individual T-O-T angles, not reported here but available upon request to the authors, show no significant deviation from the values described by Gualtieri et al. (1998), Ballirano et al. (2009), and Giacobbe et al. (2023).

Regarding the extraframework cations, their disordered distribution and the presence of nearly isoelectronic species required the use of prior information on the chemical composition and the expected coordination of the cations to locate them. The species were hence assigned based on the coordination and the distances from the surrounding oxygen atoms of the framework

and water molecules of the candidate cations, taking advantage of the EPMA chemical data. The cancrinite cage hosts the K1 atomic position with nearly a full site occupancy (Online Materials¹ Table S3) and a 12-fold coordination with six oxygen O2 atoms and six oxygen O3 atoms (Table 2). This site in the special position $0\ 0\ \frac{1}{4}$ is a key templating agent of the erionite framework because it is invariably present and almost fully occupied by K⁺ in the cancrinite cage of all the natural erionite structure models from the literature regardless of their composition (erionite-Ca, erionite-Na, or erionite-K). With the exception of Ballirano et al. (2009) for erionite-K from Oregon, all the natural erionite structure models report a 12-fold coordination with a group of six shorter distances from the framework oxygen O2 atoms and six longer distances from the oxygen O3 atoms (Alberti et al. 1997; Gualtieri et al. 1998, 2016; Cametti et al. 2013; Quiroz-Estrada et al. 2020; Battiston et al. 2022; Giacobbe et al. 2023; Mattioli et al. 2023). When the value of the K1-O2 distances are close to the value of the K1-O3 distances, like in our erionite structure, the coordination sphere is more symmetrical, resembling a spherical shape (see Fig. 8a). On the other hand, when the value of the K1-O2 distances departs from the value of the K1-O3 distances, as observed for other erionite structure models, the coordination gets closer to a hexagonal prism with two layers of oxygen atoms at more or less the same height (see **b** in Fig. 8). Other K⁺ atoms were located in the big erionite cavity in correspondence with the K2 and K3 special positions at 0.5 0 0 and $\frac{1}{3}\ \frac{2}{3}\ 0.1135$, respectively. Again, K⁺ atoms display a 12-fold coordination with both framework oxygen atoms and H₂O molecules (see Table 2, considering that 2 out of 4 OW3 sites are mutually exclusive). It is the first time that residual K⁺ is refined in a position different from K2. In fact, literature data invariably reports residual K⁺, if found, in the K2 site in the erionite cavity (Ballirano et al. 2009; Battiston et al. 2022; Giacobbe et al. 2023; Mattioli et al. 2023) with a distorted 12-fold coordination of framework oxygen atoms and H₂O molecules. The refined position K3 corresponds to the Ca2 site in Alberti et al. (1997), Ballirano et al. (2009), Cametti et al. (2013), Gualtieri et al. (2016), Quiroz-Estrada et al. (2020), Battiston et al. (2022), and Mattioli et al. (2023). K3

FIGURE 8. Representation of the 12-fold coordination environment of K⁺ inside the cancrinite cage. (a) When the value of the 6 K1-O2 distances is close to the value of the 6 K1-O3 distances, like in GD4a erionite, the coordination sphere is more symmetrical, resembling a spherical shape. (b) When the value of the 6 K1-O2 distances departs from the value of the 6 K1-O3 distances, like in other erionite structure models (e.g., Giacobbe et al. 2023), the coordination gets closer to a hexagonal prism with two layers of oxygen atoms at more or less the same height along the c axis.



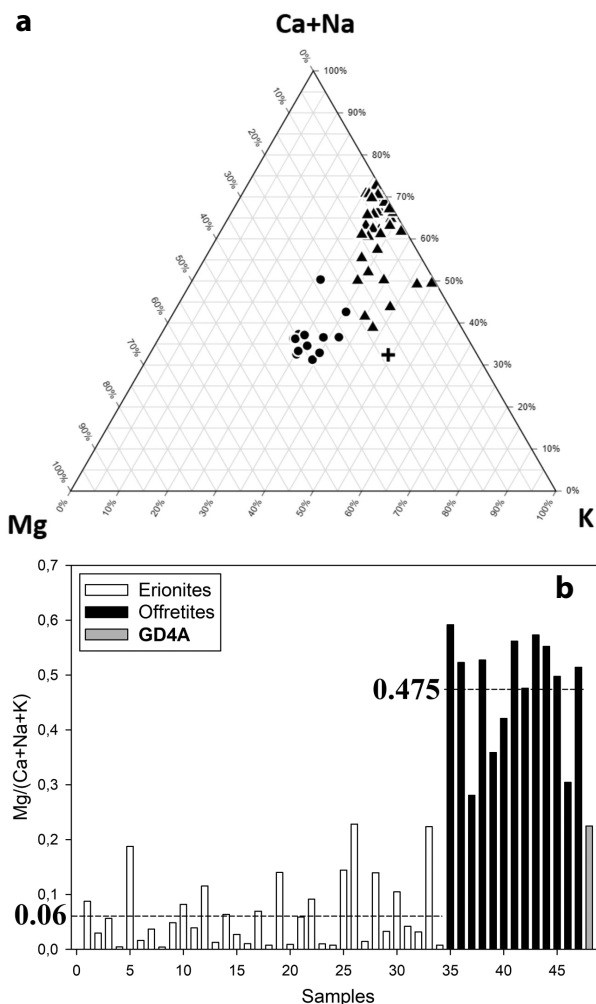


FIGURE 9. (a) Compositional diagram showing the extraframework cation content of erionite and offretite samples from the literature (Alberti et al. 1997; Passaglia et al. 1998; Ballirano et al. 2009; Cametti et al. 2013; Gualtieri et al. 2016; Quiroz-Estrada et al. 2020; Battiston et al. 2022; Giacobbe et al. 2023; Mattioli et al. 2023). Legend: black triangles = erionite; black circles = offretite; black cross = Gawler Downs (New Zealand), this work; (b) plot derived from the same literature data plotted in a with sample discrimination based on the calculated ratio $Mg/(Ca+Na+K)$. Legend: erionites = white bars; offretites = black bars; GD4a sample from New Zealand = gray bar.

instead corresponds to the Ca1 site in Gualtieri et al. (1998) and Giacobbe et al. (2023).

In our erionite structure model, extraframework cations other than K^+ (Ca^{2+} with minor Na^+ and Ba^{2+}) were located inside the big erionite cavity in the Ca1 and Ca2 special positions (Online Materials¹ Table S3). The refined position Ca1 corresponds to the Ca1 site in Alberti et al. (1997), Ballirano et al. (2009), Cametti et al. (2013), Gualtieri et al. (2016), Quiroz-Estrada et al. (2020), Battiston et al. (2022), and Mattioli et al. (2023). Ca1 instead corresponds to the Ca2 site in Gualtieri et al. (1998) and Giacobbe et al. (2023). A 6- to 9-fold coordination with H_2O molecules (see Table 2, considering that three out of six OW3 sites are mutually exclusive) is calculated for the Ca1 position.

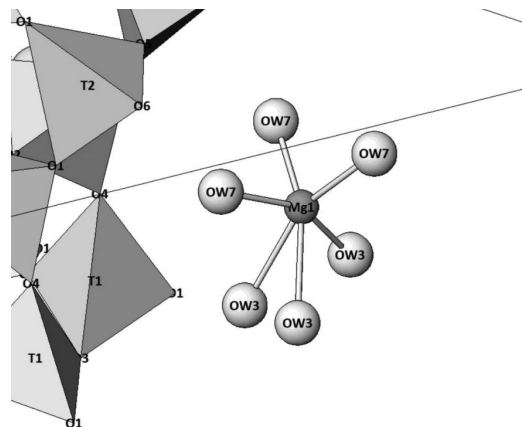


FIGURE 10. The best configuration around the Mg^{2+} in the erionite cavity showing a 6-fold coordination with 3 out of the 6 mutually exclusive H_2O molecules OW3 at 2.092 Å and 3 H_2O molecules OW7 at 1.897 Å.

When Na^+ occupies that site, the coordination number is six. The refined position Ca2 corresponds to the Ca3 site in Alberti et al. (1997), Ballirano et al. (2009), Cametti et al. (2013), Gualtieri et al. (2016), Quiroz-Estrada et al. (2020), Battiston et al. (2022), and Mattioli et al. (2023). A 9-fold coordination with H_2O molecules (see Table 2 again, considering that 3 out of 6 OW3 sites are mutually exclusive) is calculated for the Ca2 position when both Ca^{2+} and Ba^{2+} occupy that position.

Extraframework magnesium atoms deserve a dedicated discussion. Figure 9a is a standard compositional plot used to classify erionite (black triangles) and offretite (black circles) samples from the extraframework cation content. Data points are taken from the literature (Alberti et al. 1997; Gualtieri et al. 1998, 2016; Ballirano et al. 2009; Cametti et al. 2013; Quiroz-Estrada et al. 2020; Battiston et al. 2022; Giacobbe et al. 2023; Mattioli et al. 2023) and show that the asbestiform erionite from Gawler Downs (black cross) is anomalous, with a quite unique content of K^+ and Mg^{2+} . Figure 9b is a plot derived from the data plotted in Figure 9a, showing the calculated ratio $Mg/(Ca+Na+K)$ for each sample. This parameter permits better discrimination between the erionite and the offretite families. Erionites (white bars) display a mean $Mg/(Ca+Na+K) = 0.06$ with a maximum value of 0.2282. Offretites (black bars) display a mean $Mg/(Ca+Na+K) = 0.475$ with a minimum value of 0.2808. The GD4a sample from New Zealand (gray bar) displays a $Mg/(Ca+Na+K) = 0.2248$, and its inclusion in the family of erionite is fully justified. Despite the high content of magnesium in the GD4a sample, there is no evidence of offretite nor erionite-offretite disordered sequences as observed for other Mg-rich samples like the erionite from Araules (Ht. Loire, France) with $Mg = 0.83$ afu (Gualtieri et al. 1998). Mg^{2+} is located in the erionite cavity surrounded by a cloud of H_2O molecules. The best configuration is in a 6-fold coordination with three out of the six mutually exclusive H_2O molecules OW3 at 2.092 Å, and 3 H_2O molecules OW7 at 1.897 Å (Fig. 10; Table 2). Alternatively, another configuration with 3 H_2O molecules OW3 at 2.092 Å and 3 H_2O molecules OW5 at 2.423 Å is also possible but much more distorted. In agreement, a survey of the existing structure models of erionite from

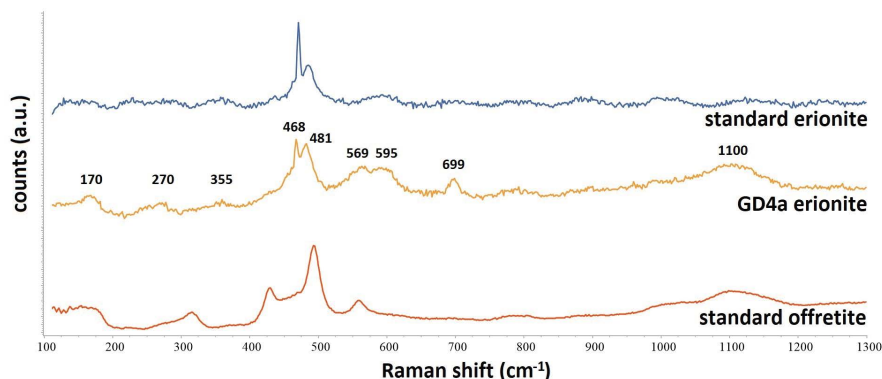
the literature shows that Mg^{2+} is mostly found inside the erionite cavity, at different heights along the principal crystallographic axis, and surrounded by 6 H_2O molecules. It is in the position corresponding to Ca2 site with 3 H_2O molecules at 1.91 Å and 3 H_2O molecules at 2.28 Å in erionite-Ca from Shourdo (Georgia) (Gualtieri et al. 1998); in the Ca2 site with 3 H_2O molecules at 2.19 Å and 3 H_2O molecules at 2.76 Å in erionite-Ca from Agate beach (Oregon, U.S.A.) (Gualtieri et al. 1998); in the Ca1 site with 3 H_2O molecules at 1.88 Å and 3 H_2O molecules at 2.68 Å in erionite-Na from Durkee (Oregon, U.S.A.) (Cametti et al. 2013); in the Ca3 site with 3 H_2O molecules at 2.20 Å and 3 H_2O molecules at 2.25 Å in erionite-K from Tuzköy (Turkey; Giacobbe et al. 2023). Crystallographic sites hosting Mg^{2+} atoms refined inside the erionite cavity but surrounded by a disordered solvation sphere of water molecules were also calculated: Ballirano et al. (2009) found evidence of Mg^{2+} in the Ca1 site with 2 H_2O molecules at 2.05, 2.16, 2.17, and 2.37 Å, respectively, in erionite-K from Rome (Oregon, U.S.A.); Quiroz-Estrada et al. (2020) refined Mg^{2+} in the Ca1 site with 3 H_2O molecules at 1.79 and 2.40 Å, respectively, and 6 H_2O molecules at 1.97 and 2.44 Å, respectively, in erionite-Na from Agua Prieta (Sonora, Mexico); Battiston et al. (2022) refined Mg^{2+} in the Ca1 site with 3 H_2O molecules at 1.86 Å and 6 H_2O molecules at 2.51 Å, respectively, in erionite-K from Chase Creek, Falkland, British Columbia (Canada); finally Mattioli et al. (2023) refined Mg^{2+} in the Ca1 site with 3 H_2O molecules at 2.22, 2.29, and 2.49 Å, respectively, in erionite-K from Poggio Nibbio (Latium, Italy). A sample from the same locality but classified as erionite-Na displayed Mg^{2+} in the Ca1 site with 3 H_2O molecules at 2.22, 2.32, 2.42, and 2.44 Å, respectively. The analysis of the coordination sphere of Mg^{2+} does not correlate with the Mg-content nor the chemical nature of the erionite sample.

Sample GD4a was also analyzed using micro-Raman with the spectrum reported in Figure 11 (middle curve). The spectrum is compared to that of a pure erionite-K from Rome, Oregon (U.S.A.; top curve) and a pure offretite from Saviole (Brescia, Italy; bottom curve) in the Raman shift region 100 to 1400 cm^{-1} (Giacobbe et al. 2023). GD4a shows bands at 170, 270, 355 (?), 468, 482, 569, 595, 699, and 1100 cm^{-1} in the investigated region. The erionite-K sample from Oregon shows bands at 355, 470, 486, and 595 cm^{-1} while the offretite sample shows bands at 140, 270 (?), 429, 467, 495, and 559 cm^{-1} . Based on the existing literature on the Raman spectroscopy of natural zeolites, it is possible to interpret the observed bands in terms of molecular vibrational modes. The weak

band at 170 cm^{-1} is tentatively assigned to the bending vibrational mode δ of the O-T-O bonds (Brémard and Le Maire 1993); the very weak bands at 270 and 355 cm^{-1} are assigned to the symmetric bending vibrational modes δ_s of the T-O-T bonds in the double 6-membered (D6R) rings and to the antisymmetric bending vibrational modes δ_a of the T-O-T bonds in the double 6-membered (D6R) rings, respectively (Wang et al. 2019); the intense bands at 467 and 486 cm^{-1} are assigned to the symmetric bending vibrational modes δ_s of the T-O-T bonds in the 6-membered rings and to the symmetric bending vibrational modes δ_s of the T-O-T bonds in the 4-membered rings, respectively (Mozgawa 2001; Croce et al. 2013); the bands at 569 and 595 cm^{-1} are tentatively assigned to the antisymmetric bending vibrational modes δ_a of the T-O-T bonds in the 6-membered rings and to the antisymmetric bending vibrational modes δ_a of the T-O-T bonds in the 4-membered rings, respectively; the band at 698 cm^{-1} is assigned to the symmetric stretching mode ν_s of the T-O bonds (Lercher and Jentys 2007); the weak band at 1100 cm^{-1} is assigned to the antisymmetric stretching mode ν_a of the T-O bonds (Giacobbe et al. 2023). The spectrum of the GD4a sample, with the major bands at 468, 482, and 569 cm^{-1} , is much closer to that of erionite-K from Oregon and the signals reported for the Tuzköy (Turkey) and Jersey (U.S.A.) fibrous erionites published by Giacobbe et al. (2023), showing the major bands at 468, 488–489, and 569–571 cm^{-1} . Rinaudo and Croce (2019) also reported that the major distinctive bands of erionite-K from Oregon are at 471, 486, and 569 cm^{-1} , supporting the interpretation that the GD4a sample is actually erionite. In fact, the GD4a sample does not show the major bands of offretite at 429 and 467 cm^{-1} (Fig. 11 bottom) observed at 431 and 465 cm^{-1} by Giacobbe et al. (2023).

Overall, the analytical techniques have determined that sample GD4a is erionite-K, with a unique composition. This is supported by the micro-Raman data spectrum, which shows very similar bands to the erionite-K standard from Oregon (Giacobbe et al. 2023). Furthermore, the sample has an asbestiform crystal habit, as seen within the SEM images, and the fibrils are in agreement with the WHO (1986, 1997) requirements for respirable fibers. TGA estimated the zeolitic water to be 17.7 wt%, a value typically seen within zeolites. The EPMA calculation for the GD4a chemical formula is also in agreement with other occurrences of erionite; however, this sample has a slightly higher Mg^{2+} content. TEM suggested the presence of layer silicates on the surface of erionite fibers and this is confirmed by XRPD data, which denotes the presence of smectite and illite.

FIGURE 11. Micro-Raman spectrum of erionite-K standard from Rome, Oregon (U.S.A.) (top), GD4a erionite sample (middle), and standard offretite from Saviole (Italy) (bottom). See text for details.



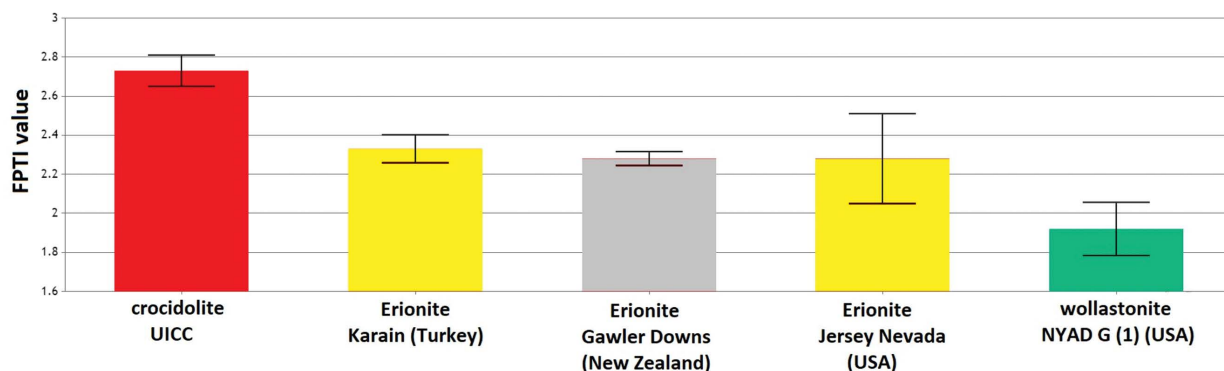


FIGURE 12. Comparison of the value of the Fiber Potential toxicity Index (FPTI) of GD4a erionite with those of other asbestiform erionites, a positive standard UICC crocidolite and a negative standard NYAD G wollastonite. The values are calculated using the online application available at <http://fibers-fpti.unimore.it/FPTI/> (Gualtieri et al. 2021). See the text for details.

MODEL OF POTENTIAL TOXICITY/CARCINOGENICITY

To assess the potential toxicity/carcinogenicity of the asbestiform erionite GD4a sample, we used the FPTI model (Gualtieri 2018, 2021) which has been applied to a suite of mineral fibers [e.g., fibrous glaucophane (Di Giuseppe et al. 2019), Russian chrysotile (Di Giuseppe et al. 2021a)] in the attempt to predict their ability to induce adverse effects in vitro/in vivo (Mossman and Gualtieri 2020). For the calculation, the model considers all the physical-crystal-chemical parameters responsible for adverse effects, including morphometric parameters, chemical parameters, biodurability-related parameters, and surface reactivity.

In terms of morphometric parameters, a key factor of carcinogenicity is the length and width of the erionite fibers (Gualtieri 2018, 2021). Images from SEM and TEM have displayed that sample GD4a is made up of thick fibers (mean $\sim 12.07 \mu\text{m}$) split into nanometric fibrils with a mean width of $1.36 \mu\text{m}$ (SEM), and $0.39 \mu\text{m}$ (TEM), the length is $206 \mu\text{m}$. The fibers are not respirable, however, if the sample splits into much smaller respirable fibrils, they could potentially be carcinogenic due to their $\leq 3 \mu\text{m}$ diameter and $\geq 3:1$ length-to-width ratio (mean ratio is $171 \mu\text{m}$; see Table 1). The splitting of the fibers has also resulted in a higher surface area to volume ratio, which can increase the surface reactivity of the sample (Dogan et al. 2008; Gualtieri 2023). Regarding chemical parameters, the sample from Gawler Downs contains no iron within its chemical structure; iron exists only in the form of layer silicates on the surface of the fibers, negating some of the toxic effects that may occur (Gualtieri 2018). More detailed information on the data set used for the FPTI calculation can be found in Online Materials¹ S4, which shows the exact values used for the calculation.

The FPTI value calculated for the GD4a sample is 2.28(4). This value must be compared to those available for other asbestiform fibrous-erionites from Karain (Turkey: Lowers et al. 2010) and Jersey (Nevada, U.S.A.: Gualtieri et al. 2016), a positive carcinogenic standard UICC crocidolite (Gualtieri 2012) and the negative (non-carcinogenic) standard NYAD G (1) wollastonite (Fig. 12; Di Giuseppe et al. 2021b). The calculated value is comparable to that of the other erionites [2.33(7) and 2.28(21) for Karain and Jersey samples, respectively], significantly lower than the value of the positive standard UICC crocidolite [2.73(8)] and well above the value of the negative wollastonite standard

[1.9(1)]. The minor difference with respect to the carcinogenic Karain fiber from Turkey is likely due to a lower content of toxic metals that can be exchanged in vitro/in vivo.

IMPLICATIONS

An important implication from this study is that erionite from Gawler Downs is a health hazard comparable to other asbestiform erionites that have been investigated in other parts of the world. This is evident by the analytical data, which displays key morphometric features compatible with carcinogenic erionite. One such key feature is the size and length of the erionite fibers. The mean width of GD4a fibers was $12.07 \mu\text{m}$, however, the mean fibril width was $1.36 \mu\text{m}$ under SEM and $0.39 \mu\text{m}$ under TEM, both of which are $\leq 3 \mu\text{m}$. The mean length of the fibrils was $206.82 \mu\text{m}$, and the L_f/W_f was 171.05 (an aspect ratio $\geq 3:1$). These dimensions indicate that the erionite fibrils if separated from the fibers, are potentially respirable according to the WHO criteria (IARC 2002; Mossman et al. 2011). Furthermore, the FPTI calculation also indicates that GD4a has a similar toxicity potential to other carcinogenic erionites. For example, the erionite from Karain, Turkey (Dogan and Dogan 2008) had a composition of erionite-K and erionite-Na, which resulted in cases of malignant mesothelioma (Dogan and Dogan 2008; Dogan et al. 2008). Although further studies are needed, there is the possibility that different types of erionite may cause a variance in toxicity. The composition of sample GD4a is most closely aligned to that of erionite-K, indicating potassium is the most abundant extra framework cation within the chemical structure, and the formula calculated with EPMA is $\text{K}_{2.63}\text{Ca}_{1.27}\text{Mg}_{0.98}\text{Na}_{0.37}\text{Ba}_{0.03}\text{Sr}_{0.01}[\text{Si}_{28.43}\text{Al}_{7.56}\text{I}_{35.99}\text{O}_{72} \cdot 29.07\text{H}_2\text{O}]$. The erionite contained a high degree of Mg^{2+} , more than what erionite typically contains. Nevertheless, further comparisons with other known erionite and offretite samples have indicated that GD4a is indeed erionite, with a unique content of K^+ and Mg^{2+} , and contains no offretite or disordered erionite-offretite sequences within the mineral.

Erionite is only a hazard when it becomes airborne due to disturbances such as erosive processes or human activities making it airborne. The erionite fibers were found to be localized to open vesicles in the andesite-dacite formation. The Gawler Downs area has a low population density and is mostly farmland,

with potential sources of disturbance to the erionite fibers being quad-biking or vegetation clearance and disturbance from foot or animal traffic, as these activities have been proven to cause the aerosolization of mineral fibers (Beaucham et al. 2018). Aeolian processes and frost heave are known to occur in the region of Gawler Downs due to its climate, and these processes have the ability to liberate mineral fibers within the landscape into the air (McGowan et al. 1996).

The results from this study have indicated that asbestiform erionite-K at Gawler Downs is composed of fibers and fibrils, some of which are within the hazardous range for mineral fibers. To quantify the health implications for this location, further work is required to determine the effect that erosional processes have on the mineral and any liberation into the air.

ACKNOWLEDGMENTS

Andrea Risplendente (University of Milan) is kindly acknowledged for help during the EPMA analytical session. We warmly thank the four anonymous referees of this work for their careful and constructive revision.

FUNDING

This work was funded by MBIE project 3721404: assessing and managing the risk of carcinogenic erionite in New Zealand. The work was also supported through a Royal Society of New Zealand Catalyst Seed grant 20-UOA-016-CSG (to M.B.) and through the University of Auckland Doctoral scholarship scheme (to J.P.). This work was also supported by the PRIN project fund “Fibres: a multidisciplinary mineralogical, crystal-chemical and biological project to amend the paradigm of toxicity and cancerogenicity of mineral fibres” (PRIN: Progetti di Ricerca di Rilevante Interesse Nazionale-Bando 2017-Prot. 20173X8WA4).

REFERENCES CITED

Alberti, A., Martucci, A., Galli, E., and Vezzalini, G. (1997) A reexamination of the crystal structure of erionite. *Zeolites*, 19, 349–352, [https://doi.org/10.1016/S0144-2449\(97\)00102-4](https://doi.org/10.1016/S0144-2449(97)00102-4).

Armbruster, T. and Gunter, M.E. (2001) Crystal structures of natural zeolites. *Reviews in Mineralogy and Geochemistry*, 45, 1–67, <https://doi.org/10.2138/rmg.2001.45.1>.

Baerlocher, C., McCusker, L.B., and Olson, D.H. (2007) ERI—P6/*mmc*. In C. Baerlocher, L.B. McCusker, and D.H. Olson, Eds., *Atlas of Zeolite Framework Types* (Sixth Edition), p. 128–129. Elsevier.

Ballirano, P. and Cametti, G. (2012) Dehydration dynamics and thermal stability of erionite-K: Experimental evidence of the “internal ionic exchange” mechanism. *Microporous and Mesoporous Materials*, 163, 160–168, <https://doi.org/10.1016/j.micromeso.2012.06.059>.

Ballirano, P., Andreozzi, G.B., Dogan, M., and Dogan, A.U. (2009) Crystal structure and iron topochemistry of erionite-K from Rome, Oregon, U.S.A. *American Mineralogist*, 94, 1262–1270, <https://doi.org/10.2138/am.2009.3163>.

Ballirano, P., Bloise, A., Gualtieri, A.F., Lezzerini, M., Pacella, A., Perchiazzi, N., Dogan, M., and Dogan, A.U. (2017) The crystal structure of mineral fibres. In A.F. Gualtieri, Ed., *Mineral Fibres: Crystal Chemistry, Chemical-Physical Properties, Biological Interaction and Toxicity*, vol. 18, p. 17–64. Mineralogical Society of Great Britain.

Barış, B., Demir, A.U., Shehu, V., Karakoca, Y., Kısacık, G., and Barış, Y.I. (1996) Environmental fibrous zeolite (erionite) exposure and malignant tumors other than mesothelioma. *Journal of Environmental Pathology, Toxicology and Oncology*, 15, 183–189.

Battiston, T., Comboni, D., Pagliaro, F., Lotti, P., Hanfland, M., and Gatta, G.D. (2022) High-pressure behavior and crystal-fluid interaction in natural erionite-K. *Materials Chemistry and Physics*, 292, 126760, <https://doi.org/10.1016/j.matchemphys.2022.126760>.

Beaucham, C., King, B., Feldmann, K., Harper, M., and Dozier, A. (2018) Assessing occupational erionite and respirable crystalline silica exposure among outdoor workers in Wyoming, South Dakota, and Montana. *Journal of Occupational and Environmental Hygiene*, 15, 455–465, <https://doi.org/10.1080/15459624.2018.1447116>.

Bloise, A., Catalano, M., Barrese, E., Gualtieri, A.F., Bursi Gandolfi, N., Capella, S., and Belluso, E. (2016) TG/DSC study of the thermal behaviour of hazardous mineral fibres. *Journal of Thermal Analysis and Calorimetry*, 123, 2225–2239, <https://doi.org/10.1007/s10973-015-4939-8>.

Bloise, A., Kusiorowski, R., Gualtieri, M.L., and Gualtieri, A.F. (2017) Thermal behaviour of mineral fibres. In A.F. Gualtieri, Ed., *Mineral Fibres: Crystal Chemistry, Chemical-Physical Properties, Biological Interaction and Toxicity*,

18, 215–260. Mineralogical Society of Great Britain.

Brémard, C. and Le Maire, M. (1993) Low-frequency Raman spectra of dehydrated faujasitic zeolites. *Journal of Physical Chemistry*, 97, 9695–9702, <https://doi.org/10.1021/j100140a028>.

Brook, M.S., Black, P.M., Salmund, J., Dirks, K.N., Berry, T.-A., and Steinhorn, G. (2020) Erionite in Auckland bedrock and malignant mesothelioma: An emerging public and occupational health hazard? *The New Zealand Medical Journal*, 133, 73–78.

Burla, M.C., Caliendo, R., Carrozzini, B., Cascarano, G.L., Cuocci, C., Giocavazzo, C., Mallamo, M., Mazzone, A., and Polidori, G. (2015) Crystal structure determination and refinement via SIR2014. *Journal of Applied Crystallography*, 48(1), 306–309, <https://doi.org/10.1107/S160057615001132>.

Cametti, G., Pacella, A., Mura, F., Rossi, M., and Ballirano, P. (2013) New morphological, chemical, and structural data of woolly erionite-Na from Durkee, Oregon, U.S.A. *American Mineralogist*, 98, 2155–2163, <https://doi.org/10.2138/am.2013.4474>.

Croce, A., Musa, M., Allegrina, M., Rinaudo, C., Baris, Y.I., Dogan, A.U., Powers, A., Rivera, Z., Bertino, P., Yang, H., and others. (2013) Micro-Raman spectroscopy identifies crocidolite and erionite fibers in tissue sections. *Journal of Raman Spectroscopy: JRS*, 44, 1440–1445, <https://doi.org/10.1002/jrs.4286>.

Di Giuseppe, D., Harper, M., Bailey, M., Erskine, B., Della Ventura, G., Ardit, M., Pasquali, L., Tomaino, G., Ray, R., Mason, H., and others. (2019) Characterization and assessment of the potential toxicity/pathogenicity of fibrous glaucofane. *Environmental Research*, 178, 108723, <https://doi.org/10.1016/j.envres.2019.108723>.

Di Giuseppe, D., Zoboli, A., Nodari, L., Pasquali, L., Sala, O., Ballirano, P., Malferrari, D., Raneri, S., Hanuskova, M., and Gualtieri, A.F. (2021a) Characterization and assessment of the potential toxicity/pathogenicity of Russian commercial chrysotile. *American Mineralogist*, 106, 1606–1621, <https://doi.org/10.2138/am-2021-7710>.

Di Giuseppe, D., Scognamiglio, V., Malferrari, D., Nodari, L., Pasquali, L., Lasinatti Gualtieri, M., Scarfi, S., Mirata, S., Tessari, U., Hanuskova, M., and others. (2021b) Characterization of fibrous wollastonite NYAD G in view of its use as negative standard for in vitro toxicity tests. *Minerals*, 11, 1378, <https://doi.org/10.3390/min11121378>.

Dogan, A.U. and Dogan, M. (2008) Re-evaluation and re-classification of erionite series minerals. *Environmental Geochemistry and Health*, 30, 355–366, <https://doi.org/10.1007/s10653-008-9163-z>.

Dogan, A.U., Dogan, M., and Hoskins, J.A. (2008) Erionite series minerals: Mineralogical and carcinogenic properties. *Environmental Geochemistry and Health*, 30, 367–381, <https://doi.org/10.1007/s10653-008-9165-x>.

Field, B.D. and Browne, G.H. (1989) Cretaceous and Cenozoic Sedimentary Basins and Geological Evolution of the Canterbury Region, South Island, New Zealand, 94 p. New Zealand Geological Survey.

Gemmi, M., Mugnaioli, E., Gorelik, T.E., Kolb, U., Palatinus, L., Boullay, P., Hovmöller, S., and Abrahams, J.P. (2019) 3D electron diffraction: The nanocrystallography revolution. *ACS Central Science*, 5, 1315–1329, <https://doi.org/10.1021/acscentsci.9b00394>.

Giacobbe, C., Moliterni, A., Di Giuseppe, D., Malferrari, D., Wright, J.P., Mattioli, M., Raneri, S., Giannini, C., Fornasini, L., Mugnaioli, E., and others. (2023) The crystal structure of the killer fibre erionite from Tuzköy (Cappadocia, Turkey). *IUCrJ*, 10, 397–410, <https://doi.org/10.1107/S2052252523003500>.

Giordani, M., Mattioli, M., Dogan, M., and Dogan, A.U. (2016) Potential carcinogenic erionite from Lessini Mounts, NE Italy: Morphological, mineralogical and chemical characterization. *Journal of Toxicology and Environmental Health, Part A*, 79, 808–824, <https://doi.org/10.1080/15287394.2016.1182453>.

Giordani, M., Mattioli, M., Ballirano, P., Pacella, A., Cenni, M., Boscardin, M., and Valentini, L. (2017) Geological occurrence, mineralogical characterization, and risk assessment of potentially carcinogenic erionite in Italy. *Journal of Toxicology and Environmental Health, Part B, Critical Reviews*, 20, 81–103, <https://doi.org/10.1080/10937404.2016.1263586>.

Giordani, M., Mattioli, M., Cangiotti, M., Fattori, A., Ottaviani, M.F., Betti, M., Ballirano, P., Pacella, A., Di Giuseppe, D., Scognamiglio, V., and others. (2022) Characterisation of potentially toxic natural fibrous zeolites by means of electron paramagnetic resonance spectroscopy and morphological-mineralogical studies. *Chemosphere*, 291, 133067, <https://doi.org/10.1016/j.chemosphere.2021.133067>.

Gottardi, G. and Galli, E. (1985) Zeolites with 6-rings. In G. Gottardi and E. Galli, Eds., *Natural Zeolites*, p. 168–222. Springer-Verlag.

Gualtieri, A.F. (2012) 7—Mineral fibre-based building materials and their health hazards. In F. Pacheco-Torgal, S. Jalali, and A. Fucic, Eds., *Toxicity of Building Materials*, p. 166–195. Woodhead Publishing.

——— (2018) Towards a quantitative model to predict the toxicity/pathogenicity potential of mineral fibres. *Toxicology and Applied Pharmacology*, 361, 89–98, <https://doi.org/10.1016/j.taap.2018.05.012>.

——— (2021) Bridging the gap between toxicity and carcinogenicity of mineral fibres by connecting the fibre crystal-chemical and physical parameters to the key characteristics of cancer. *Current Research in Toxicology*, 2, 42–52, <https://doi.org/10.1016/j.crttox.2021.01.005>.

- (2023) Journey to the centre of the lung. The perspective of a mineralogist on the carcinogenic effects of mineral fibres in the lungs. *Journal of Hazardous Materials*, 442, 130077, <https://doi.org/10.1016/j.jhazmat.2022.130077>.
- Gualtieri, A., Artioli, G., Passaglia, E., Bigi, S., Viani, A., and Hanson, J.C. (1998) Crystal structure-crystal chemistry relationships in the zeolites erionite and offretite. *American Mineralogist*, 83, 590–606, <https://doi.org/10.2138/am-1998-5-619>.
- Gualtieri, A.F., Gandolfi, N.B., Pollastri, S., Pollok, K., and Langenhorst, F. (2016) Where is iron in erionite? A multidisciplinary study on fibrous erionite-Na from Jersey (Nevada, USA). *Scientific Reports*, 6, 37981, <https://doi.org/10.1038/srep37981>.
- Gualtieri, A.F., Leoncini, M., Rinaldi, L., Zoboli, A., and Di Giuseppe, D. (2021) WebFPPT: A tool to predict the toxicity/pathogenicity of mineral fibres including asbestos. *Earth Science Informatics*, 14, 2401–2409, <https://doi.org/10.1007/s12145-021-00646-x>.
- Guldberg, M., Christensen, V.R., Perander, M., Zitois, B., Koenig, A.R., and Sebastian, K. (1998) Measurement of in-vitro fibre dissolution rate at acidic pH. *The Annals of Occupational Hygiene*, 42, 233–243, [https://doi.org/10.1016/S0003-4878\(98\)00026-X](https://doi.org/10.1016/S0003-4878(98)00026-X).
- Harada, K., Iwamoto, S., and Kihara, K. (1967) Erionite, phillipsite and gonardite in the amygdaloids of altered basalt from Maze, Niigata Prefecture, Japan. *American Mineralogist*, 52, 1785–1794.
- IARC (1997) Erionite, IARC Monographs on the evaluation of the carcinogenic risk of chemicals to humans, p. 225–239. International Agency for Research on Cancer.
- (2002) Man-made Vitreous Fibres, vol. 81. International Agency for Research on Cancer.
- Larson, A.C. and Von Dreele, R.B. (2004) General Structure Analysis System (GSAS). Los Alamos National Laboratory Report 86-748.
- Lercher, J. and Jentys, A. (2007) Infrared and Raman spectroscopy for characterizing zeolites. *Studies in Surface Science and Catalysis*, 168, 435–476, [https://doi.org/10.1016/S0167-2991\(07\)80801-9](https://doi.org/10.1016/S0167-2991(07)80801-9).
- Lowers, H., Adams, D.T., Meeker, G.P., and Nutt, C.J. (2010) Chemical and morphological comparison of erionite from Oregon, North Dakota, and Turkey. Open-File Report 2010-1286. USGS Numbered Series, U.S. Geological Survey.
- Mattioli, M., Giordani, M., Ballirano, P., Salvioli-Mariani, E., Bernardini, S., and Ventura, G.D. (2023) First occurrence, crystal-chemistry and structure of erionite, a carcinogenic fibrous zeolite, from the volcanic rocks of Latium (Italy). *Periodico di Mineralogia*, 92, 159–178.
- McCusker, L.B., Liebau, F., and Engelhardt, G. (2001) Nomenclature of structural and compositional characteristics of ordered microporous and mesoporous materials with inorganic hosts (IUPAC Recommendations 2001). *Pure and Applied Chemistry*, 73, 381–394, <https://doi.org/10.1351/pac200173020381>.
- McGowan, H.A., Sturman, A.P., and Owens, I.F. (1996) Aeolian dust transport and deposition by foehn winds in an alpine environment, Lake Tekapo, New Zealand. *Geomorphology*, 15, 135–146, [https://doi.org/10.1016/0169-555X\(95\)00123-M](https://doi.org/10.1016/0169-555X(95)00123-M).
- Mossman, B.T. and Gualtieri, A.F. (2020) Lung cancer: Mechanisms of carcinogenesis by asbestos. In S. Anttila and P. Boffetta, Eds., *Occupational Cancers*, 239–256. Springer.
- Mossman, B.T., Lippmann, M., Hesterberg, T.W., Kelsey, K.T., Barchowsky, A., and Bonner, J.C. (2011) Pulmonary endpoints (lung carcinomas and asbestosis) following inhalation exposure to asbestos. *Journal of Toxicology and Environmental Health, Part B, Critical Reviews*, 14, 76–121, <https://doi.org/10.1080/10937404.2011.556047>.
- Mozgawa, W. (2001) The relation between structure and vibrational spectra of natural zeolites. *Journal of Molecular Structure*, 596, 129–137, [https://doi.org/10.1016/S0022-2860\(01\)00741-4](https://doi.org/10.1016/S0022-2860(01)00741-4).
- Mugnaioli, E., Gorelik, T., and Kolb, U. (2009) “Ab initio” structure solution from electron diffraction data obtained by a combination of automated diffraction tomography and precession technique. *Ultramicroscopy*, 109(6), 758–765, <https://doi.org/10.1016/j.ultramicro.2009.01.011>.
- Naderi, M. (2015) Chapter Fourteen—Surface Area: Brunauer-Emmett-Teller (BET). In S. Tarleton, Ed., *Progress in Filtration and Separation*, 585–608. Academic Press.
- Oliver, P.J. (1977) The Mesozoic geology of the Mt Somers area, Canterbury: Including geochemical and palaeomagnetic studies of the Cretaceous calc-alkaline Mt Somers volcanics, 416 p. Ph.D. thesis, University of Canterbury, Christchurch, New Zealand.
- Oliver, P.J. and Keene, H.W. (1989) Sheet K36 AC and part Sheet K35. Geological map of New Zealand 1:50 000. Map (one sheet) and notes. Wellington, New Zealand. Department of Scientific and Industrial Research.
- Pacella, A., Ballirano, P., Fantauzzi, M., Rossi, A., Viti, C., Arrizza, L., Nardi, E., Caprioli, R., and Monteleale, M.R. (2021) Surface and bulk modifications of fibrous erionite in mimicked Gamble’s solution at acidic pH. *Minerals*, 11, 914, <https://doi.org/10.3390/min11090914>.
- Palatinus, L., Brázda, P., Jelínek, M., Hrdá, J., Steciuk, G., and Klementová, M. (2019) Specifics of the data processing of precession electron diffraction tomography data and their implementation in the program PETS2.0. *Acta Crystallographica Section B: Structural Science, Crystal Engineering and Materials*, 75(4), 512–522, <https://doi.org/10.1107/S2052520619007534>.
- Passaglia, E. and Sheppard, R.A. (2001) The crystal chemistry of zeolites. *Reviews in Mineralogy and Geochemistry*, 45, 69–116, <https://doi.org/10.2138/rmg.2001.45.2>.
- Passaglia, E., Artioli, G., and Gualtieri, A. (1998) Crystal chemistry of the zeolites erionite and offretite. *American Mineralogist*, 83, 577–589, <https://doi.org/10.2138/am-1998-5-618>.
- Patel, J.P. and Brook, M.S. (2021) Erionite asbestiform fibres and health risk in Aotearoa/New Zealand: A research note. *New Zealand Geographer*, nzg.12291.
- Patel, J.P., Brook, M.S., Kah, M., and Hamilton, A. (2022) Global geological occurrence and character of the carcinogenic zeolite mineral, erionite: A review. *Frontiers in Chemistry*, 10, 1066565, <https://doi.org/10.3389/fchem.2022.1066565>.
- Quiroz-Estrada, K., Pacella, A., Ballirano, P., Hernández-Espinosa, M.Á., Felipe, C., and Esparza-Schulz, M. (2020) Crystal chemical and structural characterization of natural and cation-exchanged Mexican erionite. *Minerals*, 10, 772, <https://doi.org/10.3390/min10090772>.
- Rietveld, H.M. (1969) A profile refinement method for nuclear and magnetic structures. *Journal of Applied Crystallography*, 2, 65–71, <https://doi.org/10.1107/S0021889869006558>.
- Rinaudo, C. and Croce, A. (2019) Micro-Raman spectroscopy, a powerful technique allowing sure identification and complete characterization of asbestiform minerals. *Applied Sciences (Basel, Switzerland)*, 9, 3092, <https://doi.org/10.3390/app9153092>.
- Schlenker, J.L., Pluth, J.J., and Smith, J.V. (1977) Dehydrated natural erionite with stacking faults of the offretite type. *Acta Crystallographica. Section B, Structural Crystallography and Crystal Chemistry*, 33, 3265–3268, <https://doi.org/10.1107/S0567740877010784>.
- Smith, T.R. and Cole, J.W. (1996) Stratigraphic and petrological variation of the Mount Somers Volcanics Group, mid Canterbury, New Zealand. *New Zealand Journal of Geology and Geophysics*, 39, 445–460, <https://doi.org/10.1080/00288306.1996.9514725>.
- Staples, L.W. and Gard, J.A. (1959) The fibrous zeolite erionite; its occurrence, unit cell, and structure. *Mineralogical Magazine and Journal of the Mineralogical Society*, 32, 261–281, <https://doi.org/10.1180/minmag.1959.032.247.01>.
- Tappenden, V.E. (2003) Magmatic response to the evolving New Zealand Margin of Gondwana during the Mid-Late Cretaceous. Ph.D. thesis, University of Canterbury, Christchurch, New Zealand.
- Toby, B.H. (2001) EXPGUI, a graphical user interface for GSAS. *Journal of Applied Crystallography*, 34, 210–213, <https://doi.org/10.1107/S0021889801002242>.
- van der Meer, Q.H.A., Waight, T.E., Whitehouse, M.J., and Andersen, T. (2017) Age and petrogenetic constraints on the lower glassy ignimbrite of the Mount Somers Volcanic Group, New Zealand. *New Zealand Journal of Geology and Geophysics*, 60, 209–219, <https://doi.org/10.1080/00288306.2017.1307232>.
- Van Gosen, B.S., Blitz, T.A., Plumlee, G.S., Meeker, G.P., and Pierson, M.P. (2013) Geologic occurrences of erionite in the United States: An emerging national public health concern for respiratory disease. *Environmental Geochemistry and Health*, 35, 419–430, <https://doi.org/10.1007/s10653-012-9504-9>.
- Wang, T., Luo, S., Tompsett, G.A., Timko, M.T., Fan, W., and Auerbach, S.M. (2019) Critical role of tricyclic bridges including neighboring rings for understanding Raman spectra of zeolites. *Journal of the American Chemical Society*, 141, 20318–20324, <https://doi.org/10.1021/jacs.9b10346>.
- WHO (1986) Asbestos and Other Natural Mineral Fibers. United Nations Environment Programme. International Labour Organisation, World Health Organization.
- (1997) Determination of airborne fibre number concentrations: a recommended method, by phase-contrast optical microscopy (membrane filter method). World Health Organization.
- Wylie, A.G. (2017) Asbestos and fibrous erionite. In J.R. Testa, Ed., *Asbestos and Mesothelioma*, p. 11–41. Springer.

MANUSCRIPT RECEIVED SEPTEMBER 7, 2023

MANUSCRIPT ACCEPTED FEBRUARY 14, 2024

ACCEPTED MANUSCRIPT ONLINE FEBRUARY 21, 2024

MANUSCRIPT HANDLED BY PAOLO LOTTI

Endnote:

¹Deposit item AM-24-99184. Online Materials are free to all readers. Go online, via the table of contents or article view, and find the tab or link for supplemental materials. The CIF has been peer-reviewed by our Technical Editors.